Direct numerical simulation of sediment entrainment in turbulent channel flow

Ji, C; Munjiza, A; AVITAL, E; Ma, J; Williams, JJR

AIP | Physics of Fluids

Direct numerical simulation of sediment entrainment in turbulent channel flow

C. Ji, A. Munjiza, E. Avital, J. Ma, and J. J. R. Williams

Citation: Physics of Fluids (1994-present) **25**, 056601 (2013); doi: 10.1063/1.4807075
View online: http://dx.doi.org/10.1063/1.4807075
View Table of Contents: http://scitation.aip.org/content/aip/journal/pof2/25/5?ver=pdfcov
Published by the AIP Publishing

Articles you may be interested in

Numerical simulation of turbulent sediment transport, from bed load to saltation
Phys. Fluids **24**, 103306 (2012); 10.1063/1.4757662

Plane Poiseuille flow of a sedimenting suspension of Brownian hard-sphere particles: Hydrodynamic stability and direct numerical simulations
Phys. Fluids **18**, 054103 (2006); 10.1063/1.2199493

Mechanisms of particle deposition in a fully developed turbulent open channel flow
Phys. Fluids **15**, 763 (2003); 10.1063/1.1545473

Numerical simulation of particle-laden turbulent channel flow
Phys. Fluids **13**, 2957 (2001); 10.1063/1.1396846

Direct numerical simulations of bubble-laden turbulent flows using the two-fluid formulation
Phys. Fluids **10**, 685 (1998); 10.1063/1.869594

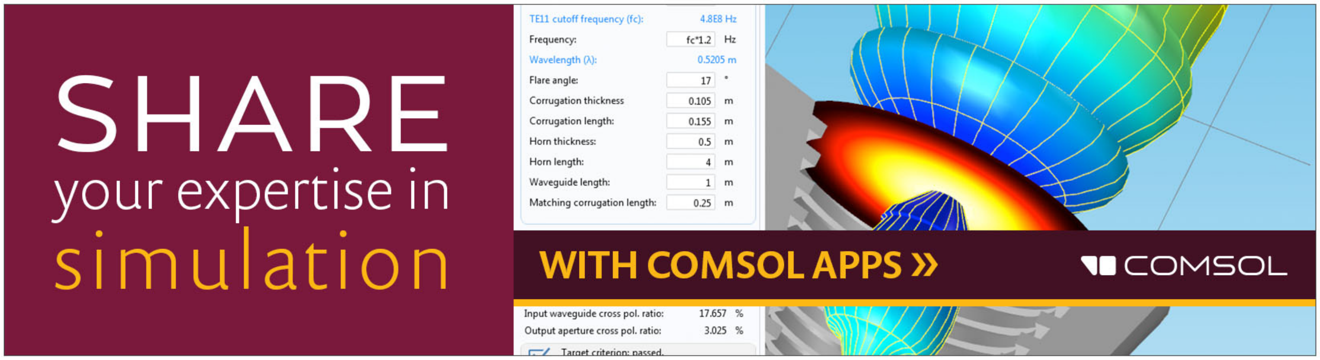
TE11 cutoff frequency (fc): 4.8E8 Hz
Frequency: fc*1.2 Hz
Wavelength (λ): 0.5205 m
Flare angle: 17 °
Corrugation thickness: 0.105 m
Corrugation length: 0.155 m
Horn thickness: 0.5 m
Horn length: 4 m
Waveguide length: 1 m
Matching corrugation length: 0.25 m
Input waveguide cross pol. ratio: 17.657 %
Output aperture cross pol. ratio: 3.025 %
Target criterion: passed.

This article is copyrighted as indicated in the article. Reuse of AIP content is subject to the terms at: http://scitation.aip.org/termsconditions. Downloaded to IP: 138.37.43.153 On: Mon, 01 Jun 2015 12:47:52

PHYSICS OF FLUIDS **25**, 056601 (2013)

Direct numerical simulation of sediment entrainment in turbulent channel flow

C. Ji,[1] A. Munjiza,[2] E. Avital,[2] J. Ma,[2] and J. J. R. Williams[2,a)]
[1]*State Key Laboratory of Hydraulic Engineering Simulation and Safety, Tianjin University, Weijin Rd., Tianjin 300072, People's Republic of China*
[2]*School of Engineering and Materials Science, Queen Mary University of London, Mile End Rd., London E1 4NS, United Kingdom*

(Received 2 November 2012; accepted 1 May 2013; published online 23 May 2013)

In this paper, the entrainment and movement of coarse particles on the bed of an open channel is numerically investigated. Rather than model the sediment transport using a concentration concept, this study treats the sediment as individual particles and investigates the interaction between turbulent coherent structures and particle entrainment. The applied methodology is a combination of the direct numerical simulation of turbulent flow, the combined finite-discrete element modeling of particle motion and collision, and the immersed boundary method for the fluid-solid interaction. In this study, flow over a water-worked rough-bed consisting of 2-3 layers of densely packed spheres is adopted and the Shields function is 0.065 which is just above the entrainment threshold to give a bed-load regime. Numerical results for turbulent flow, sediment entrainment statistics, hydrodynamic forces acting on the particles, and the interaction between turbulence coherent structures and particle entrainment are presented. It is shown that the presence of entrained particles significantly modifies the mean velocity and turbulence quantity profiles in the vicinity of a rough-bed and that the instantaneous lift force can be larger than a particle's submerged weight in a narrow region above the effective bed location, although the mean lift force is always smaller than the submerged weight. This, from a hydrodynamic point of view, presents strong evidence for a close cause-and-effect relationship between coherent structures and sediment entrainment. Furthermore, instantaneous numerical results on particle entrainment and the surrounding turbulent flow are reported which show a strong correlation between sediment entrainment and sweep events and the underlying mechanisms are discussed. © *2013 AIP Publishing LLC*. [http://dx.doi.org/10.1063/1.4807075]

I. INTRODUCTION

Sediment transport is important for predicting the impact of human intervention in river and coastal systems, which can have large and small-scale, and near and far-field consequences. Although it is generally agreed that wall-generated turbulent bursts are the primary reason for the entrainment and transport of sediment particles,[1–3] the exact mechanism is still not clear. Depending upon the size of the particles, two distinct entrainment patterns exist. When the grain-size is much smaller than the scale of the smallest eddy in the turbulent flow, the particles negligibly affect the flow field and drift with the flow passively. Niño and García[4] claimed in their experimental work with an open channel using particle and dye visualization techniques, that the particles are first entrained from the bed by ejection events and then rise towards the outer regions by the core of the shear layer. Lelouvetel *et al.*[5] experimentally showed, using simultaneous particle image velocimetry (PIV) for

---

[a)] Electronic mail: j.j.r.williams@qmul.ac.uk.

the fluid flow and particle tracking velocimetry (PTV) for the solid phase, that particle movement away from the wall is correlated with strong ejection events.

On the other hand, when the particle grain-size is large enough, e.g., when the particle diameter is larger than 100 wall units, the interaction between the particle movement and the coherent flow structures cannot be ignored. Hofland[6] used a PIV system to measure the flow field over a natural granular bed consisting of 2-3 layers of irregular gravel with a sieve diameter of 2.5-4.0 cm. He claimed that a particle is first lifted up by the upward flow caused by the clockwise rotating (in the span-wise direction) vortex of ejection structures and then entrained by the high stream-wise velocity of sweep structures. Cameron[7] measured the entrainment of spherical particles with a diameter of 4.0 cm using the PIV technique. Contrary to Hofland's conclusions, he found that the particles tend to remain stationary until strong sweep structures reach them. Dwivedi *et al.*[8] experimentally studied the relationship between coherent flow structures and the hydrodynamic forces leading to entrainment of spherical particles in turbulent channel flow. In their tests, the hydrodynamic forces on an instrumented sphere with different protrusions and the turbulent flow field were measured simultaneously and their results showed that the high lift forces which cause particle entrainment are correlated with sweep structures. Dwivedi *et al.*[9] further studied the entrainment of a movable sphere in a laboratory flume and found that the inception of particle motion is highly correlated with large sweep structures for both shielded and exposed particles.

Owing to the significant development of high-performance computers and numerical schemes, numerical simulation presents an effective way to elucidate the underlying physical mechanisms of sediment entrainment—something that is very difficult, if not impossible, to adequately measure experimentally. Using large eddy simulation (LES), Chang and Scotti[10,11] numerically investigated the hydrodynamics of individual particles driven by turbulent flow. For their one-way coupling simulations, the flow was not affected by the particle dynamics because of the small grain-size. Vinkovic *et al.*[12] numerically investigated particle entrainment and ejection events using direct numerical simulation (DNS) and the one-way coupling technique. Their results confirmed the preferential concentration of small solid particles in low-speed streaks and a normalized threshold for particle segregation was established. Escauriaza and Sotiropoulos[13] studied the mechanisms of bed-load sediment transport in turbulent junction flows using detached eddy simulation (DES) and the one-way coupling approach. They found that clusters of small particles are initially entrained by ejection flow structures and then subsequently move—either saltating or sliding along the bed. Those particles that are not entrained into suspension aggregated along quasi-stream-wise low-velocity streaks.

The main deficiency of one-way coupling simulations is that they do not take account of the interaction between the turbulent flow and particle motion. For small grain-sizes this is understandable but for larger particles, the one-way coupling approach may lead to unexpected results. However, two-way coupling simulations of individual particles on the bed of a turbulent channel is particularly difficult because it not only involves the correct modeling of the turbulence but also the movement of the particles themselves which requires the correct modeling of their dynamics and surface stresses to accurately simulate their entrainment and movement through, and effect on, the surrounding turbulent flow. Such a numerical scheme would also involve taking into account possible collisions of particles and their "shielding" and imbrication by other particles on the bed, all of which will evidently increase the difficulty of numerically simulating the problem.

This study focuses on the influence of turbulent coherent structures on the entrainment of coarse particles in an open channel. In order to do this we apply a two-way coupling approach which couples the DNS for the turbulent flow, the combined finite-discrete element method (FDEM) for the particle dynamics, and the immersed boundary method (IBM) for the fluid solid interactions. Chan-Braun *et al.*[14] used a similar methodology to numerically investigated the hydrodynamic forces and torques on spherical particles on a rough-bed consisting of one layer of spheres in a square arrangement using a combination of DNS and IBM. The same authors[15] further studied the statistical features of the sediment entrainment in a channel with a rough-bed in which the particles are small and in a suspended-load regime. In their studies, the particles were idealized as rigid spheres and their motion was determined by Newton's equations for translational and rotational rigid-body motion. Particle collisions and the resulting contact forces were calculated using the artificial repulsion potential method of Glowinski *et al.*[16] in which the normal particle-particle repulsive force was calculated using a penalty parameter. However, the tangential force (and corresponding torque) due to the frictional-sliding contact was neglected. This force can have significant effects on the particle motion and dynamics in many aspects, e.g., it can change the hydrodynamic lift force through the well-known Magnus effect. These effects can be further significant for a bed-load transport simulation due to the fact that the collision likelihood is relatively higher. In the present study a more accurate approach was taken in which the particle deformability, frictional contact forces, and frictional and plastic-loss of energy was taken into account by applying FDEM.

II. METHODOLOGY

A. General description

The problem can be divided into three sub-problems, i.e., the simulation of turbulent channel flow, the simulation of particle movement, deformation and collision, and the simulation of the interaction between turbulent flow and particle motion. Accordingly, the methodology applied in this study is a combination of three cutting-edge numerical technologies and the corresponding computing codes.

The code used to simulate the turbulent flow is an in-house 3D DNS/LES computational fluid dynamics (CFD) C code called CgLes—see Thomas and Williams[17]—with second-order accuracy in both time and space. This code was applied to simulate turbulent flow over a rough-bed in the authors previous work[18,19] and has a proven high fidelity and parallelizing efficiency.

The immersed boundary method, first introduced by Peskin[20] for the simulation of blood flow around the flexible leaflet of the human heart, has been incorporated into CgLes to model the interaction between the flow and moving particles. One of the main advantages of the IBM is its inherent simplicity in treating flows which have solids with moving boundaries and, in order to improve its accuracy, the iterative direct-forcing version developed by Ji *et al.*[21] was utilized in this study.

To simulate the movement and collision of particles, we coupled CgLes with another in-house C code developed by Munjiza *et al.*[22] This combined finite-discrete element modeling code comprises a set of C libraries incorporating the latest breakthroughs in discontinua simulations and is capable of modeling the movement and collisions of millions of particles of different shape and size.

For the sake of conciseness, details of the methodology, except the collision strategy, are not presented here and readers should refer to previous work[17,18,21–23] for further information and validations.

B. Collision strategy

When dealing with particle systems, either wet or dry, it is important to properly resolve the contacts or collisions between the particles. In the context of FDEM, each particle of general shape is represented as a single discrete element which is then discretized into finite elements for deformability, fracture, and fragmentation. The penalty function method is employed to calculate the normal contact force $\mathbf{f}_n$ when two particles are in contact and assumes that the two particles penetrate each other. Because the discrete elements are discretized into finite elements, each contacting pair of discrete elements is in fact represented by a set of contacting finite elements. The elemental contact force is then directly related to the overlapping area of the finite elements in contact. In this study, a distributed contact force algorithm introduced by Munjiza and Andrews[24]—which is relatively easy to implement and preserves energy balance—is applied to generate a realistic distribution of contact forces over finite contact areas. The calculated elemental contact force is then distributed around the nodes surrounding the contact in order to preserve the system from artificial stress concentration.

As suggested by Munjiza and Andrews,[24] the normal contact force is given by

$$\mathbf{f}_n = \sum_{i=1}^{n} \sum_{j=1}^{m} \int_{\Gamma_{\beta_{ci} \cap \beta_{tj}}} \mathbf{n}_{\Gamma_{\beta_{ci} \cap \beta_{tj}}} (\varphi_{ci} - \varphi_{tj}) d\Gamma, \tag{1}$$

where β_{ci} and β_{tj} are the *i*th and *j*th finite elements of the contactor and target discrete elements, respectively, while *n* and *m* are the total number of finite elements into which the contactor and target discrete elements are discretized. $\mathbf{n}$ is the outward unit normal to the boundary Γ of the overlapping volume $\beta_{ci} \cap \beta_{tj}$. φ_c and φ_t are potential functions for the contactor and target discrete elements, respectively.

In this study, the simplest finite element in 3D—a linear four-node tetrahedron—has been adopted. The potential function at an arbitrary point *p* inside a tetrahedral finite element is given by

$$\varphi(p) = k_p \min\{4V_1/V,\ 4V_2/V,\ 4V_3/V,\ 4V_4/V\}, \tag{2}$$

where k_p is the penalty parameter, V is the volume of the tetrahedral finite element, and V_i ($i = 1, 2, 3, 4$) are the volumes of the corresponding sub-tetrahedrons at the point *p*. The potential φ equals 1 at the tetrahedron center and 0 at and beyond the tetrahedron surfaces.

Xiang *et al.*[23] further developed the FDEM method by taking into account the sliding friction force by implementing the well-known Coulomb-type friction described as follows:

$$\mathbf{f}_t = -k_t \mathbf{d}_t - \eta_d \mathbf{v}_t, \tag{3}$$

in which $\mathbf{f}_t$ is the tangential elastic contact force, k_t is the tangential spring stiffness constant, η_d is the viscous damping coefficient, and $\mathbf{d}_t$ and $\mathbf{v}_t$ are the tangential relative displacement and velocity between particles, respectively. If $\mathbf{f}_t$ is bigger than the friction force obeying the Coulomb-type friction law, i.e., $|\mathbf{f}_t| > \mu|\mathbf{f}_n|$, the particles slide over one another and the tangential force is then calculated using the total normal elastic contact force $\mathbf{f}_n$:

$$\mathbf{f}_t = -\mu\, |\mathbf{f}_n|\, (\mathbf{v}_t/\, |\mathbf{v}_t|), \tag{4}$$

where μ is the coefficient of sliding friction.

The FDEM code therefore includes algorithmic procedures for deformability of individual discrete elements, fracture and fragmentation algorithms (switched off for this study), contact detection between moving solids, frictional-sliding interaction between solids, and a whole set of application specific algorithms. Readers should refer to Munjiza[25] and Munjiza *et al.*[26] for further details on the FDEM.

C. Lubrication effects

The interstitial film in the gap of colliding particles generates viscous and pressure resistances which prevent particles from touching. Fully resolving this interstitial film requires the grid spacing to be extremely small, even the body-fitted approaches will be computationally prohibitive for 3D simulations with a large number of particles. Instead, an analytical lubrication model is usually used to take into account this lubrication effect by imposing a singular lubrication force on the particles. Proper account of the micro-scale lubrication effect is essential to correctly calculate the particle viscous momentum losses during collisions for smooth particles at low and intermediate Stokes numbers calculated as $St = (\rho_s/9\rho_f)Re$. It is well known that below a Stokes number of 10 no rebound occurs after collision in viscous fluids. However, as stated in Ardekani and Rangel,[27] for collisions characterized with a Stokes number larger than 500, the restitution coefficient *e* asymptotes to that for a dry collision e_{dry} which indicates that the lubrication forces can be neglected. Simeonov and Calantoni[28] numerically investigated the mechanical and lubrication forces on colliding particles at low and intermediate Stokes numbers. In their low-*St* results with $St = 6.8$ and $e = 0.08$, 97% of the momentum loss was due to the contribution from the lubrication force. However, in their intermediate-*St* results with $St = 45$ and $e = 0.58$, the contribution to the losses of momentum from the grid-resolved pressure and viscous resistances was comparable to that from the analytically modeled lubrication force. In our study, the Stokes number is approximately 146 regarding the mean incident velocity of colliding particles roughly equals 5 times of u_τ, and thus the contribution to the momentum loss from the lubrication force should be less important. Moreover, Simeonov and Calantoni[28] found in their intermediate-*St* simulation that the magnitude of the mechanical force during particle collisions is approximately 25 times larger than that of the lubrication force. They also found that during the mechanical contact the total hydrodynamic force is dominated by the

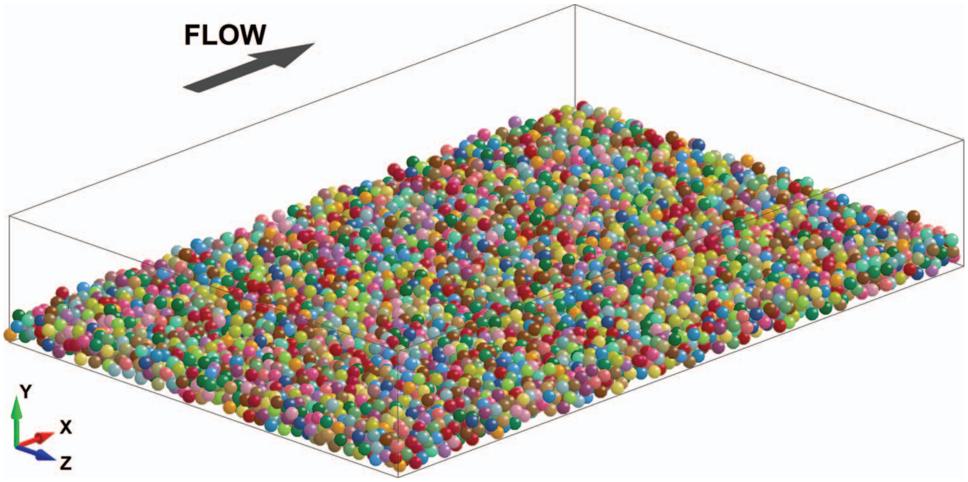

FIG. 1. Channel geometry. The domain size is $6d \times d \times 4d$ in x, y, and z directions, where d is the channel depth.

grid-resolved pressure term instead of the lubrication one. Finally, it should be noted that the surface of the natural sediment particles is by no means smooth. Surface roughness has a significant effect on the coefficient of restitution due to the fact that the lubrication film can be as thin as the height of the surface roughness, and consequently, mechanical contact may have occurred through micro-scope surface imperfections before the lubrication force become effective. This is also true in the numerical simulations of particle collisions in a viscous fluid because each particle is represented by a whole set of finite elements and thus not a perfect sphere. Point-surface contacts dominate the particle collisions and thus lubrication effects are rather weak.

Due to the reasons discussed above and for the sake of algorithm simplicity, the lubrication force is not considered in this study and it is believed that this treatment will not introduce significant errors.

III. RESULTS AND DISCUSSIONS

A. Simulation description

The entrainment of 2-3 layers of densely packed but randomly arranged spheres (see Fig. 1) in a fully developed turbulent open channel flow was investigated. The total number of spheres was 6355 and the rough-bed arrangement, which was provided by researchers in TU Delft,[6] was water-worked in that the most exposed spheres were removed. No-slip boundary conditions were used both on the bed and sphere surfaces and the top boundary was set as a free-slip hard lid. Periodicity was imposed both in the stream-wise and span-wise directions. The following list summarizes the flow simulation parameters:

- Computational box: $6d \times d \times 4d$;
- Reynolds number: $Re_d^+ = u_\tau d/\nu = 1000$;
- DNS grid: $960 \times 160 \times 640$;
- Grid resolution: $\Delta x^+ = \Delta y^+ = \Delta z^+ = 6.25$;
- Kolmogorov length scale: $\eta^+ \approx 3.3$;
- Height of roughness elements: $k = 0.3d$;
- Density ratio: $s_s = \rho_s/\rho_f = 2.65$;
- Particle diameter: $D = 0.1d$;
- Particle Reynolds number: $Re_D^+ = u_\tau D/\nu = 100$;
- Shields function: $\Theta = \tau_{eff}/((\rho_s - \rho_f)gD) = 0.065$.

In the above, d is the channel depth, u_τ is the friction velocity, τ_{eff} is the bed shear stress on the effective bed location, ν is the fluid kinematic viscosity, g is the gravitational acceleration, superscript $^+$ indicates quantities in wall units, ρ_s and ρ_f are the density of fluid and solid, respectively.

The following collision coefficients were adopted in this study. The Young's modulus is $E = 10\,\text{MPa}$, the Poisson ratio $\gamma = 0.3$, the particle density $\rho_s = 2650\,\text{kg/m}^3$, the coefficient of sliding friction $\mu = 0.4$ and the particle diameter is $D = 0.001\text{m}$. The penalty parameter is calculated as $k_p = 10E$ and the viscous contact damping is determined as $\eta_d = 2h_e\sqrt{E\rho_s}$, where h_e is the smallest size of the finite elements. Note that the value of the Young's modulus used here is rather lower than the realistic one, e.g., E for sand is typically 10–70 GPa. However, a large value of E will lead to an extremely small time step due to contact detection and computational stability, which is a significant limitation to large-scale simulations. It is shown in Simeonov and Calantoni[28] that the dynamics of granular flows is rather insensitive to the value of E and their results show that the difference is less than 4% in the coefficient of restitution for material stiffness, estimated as $ED/2$, in the range of 10^3–10^6 N/m.

The computations were run on the UK's national super-computing facility, HECToR, using 150 AMD Opteron 2.3 GHz processors for a total wall-clock time of two months, which is about 200k CPU hours. It should be mentioned here that the grid resolution in all three directions is 6.25 wall units which means that the DNS of turbulent flow is under-resolved near the wall and near the surface of the spheres. The limitations of this simulation are acknowledged and one with a finer grid will be carried out in the future.

In order to keep the computational requirements to a minimum, a LES at one half of the above-mentioned DNS grid resolution with fixed spheres was first carried out. This was run for around $30T$ (where $T = d/u_\tau$ is the large-eddy turnover time) to obtain a fully developed turbulent field which was then interpolated onto the DNS grid to yield the initial conditions for the DNS. The simulation was then continued for a further $20T$ to obtain a fully developed flow field before statistical properties were then calculated over a further $10T$.

B. Statistical features of the fixed rough-bed flow

To verify the results, the temporal and plane-averaged statistics obtained from the DNS were compared with the experimental data of Grass,[29] Nezu,[30] Grass *et al.*[31] and Defina[32] in addition to the numerical results of Singh *et al.*[18]

The effective bed location y_b and equivalent bed roughness k_s were determined by fitting the mean velocity curve to the logarithmic law-of-the-wall. y_b and k_s were calculated to be $0.84k$ and $0.807k$, respectively, by solving a two parameter nonlinear curve-fitting problem using the least squares and Newton-Raphson techniques. This, in turn, gave the roughness Reynolds number for the simulation of $k_s^+ = 242$ and, hence, a completely rough flow regime. This set of values is in agreement with the experimental data ($y_b = 0.783k$ and $k_s = 0.88k$ with $k_s^+ = 79.2$) of Defina[32] and the numerical results ($y_b = 0.81k$ and $k_s = 0.768k$ with $k_s^+ = 102$) of Singh *et al.*[18] The distance between the effective bed location and the highest crest of the roughness elements in this simulation is $\delta = 0.16k$ which is close to the lower bound of the suggested range $\delta = 0.15$–$0.3k$ of Nezu and Nakagawa.[33] Table I lists the effective flow depth $h = d - y_b$ together with other mean properties.

TABLE I. Mean flow features obtained from the DNS data for the single-phase flow.

Flow variables	Related Reynolds number
Equivalent roughness, $k_s = 0.807k$[a]	$k_s^+ = k_s u_\tau/\nu = 242$
Effective channel depth, $h = d - y_b = 2.493k$	$Re_h^+ = u_\tau h/\nu = 748$
Bulk mean velocity, $U_b = 8.578u_\tau$	$Re_b^+ = U_b h/\nu = 6417$
Mean velocity of the top surface, $U_c = 10.80u_\tau$	$Re_c^+ = U_c h/\nu = 8078$

[a] $k = 0.3d$.

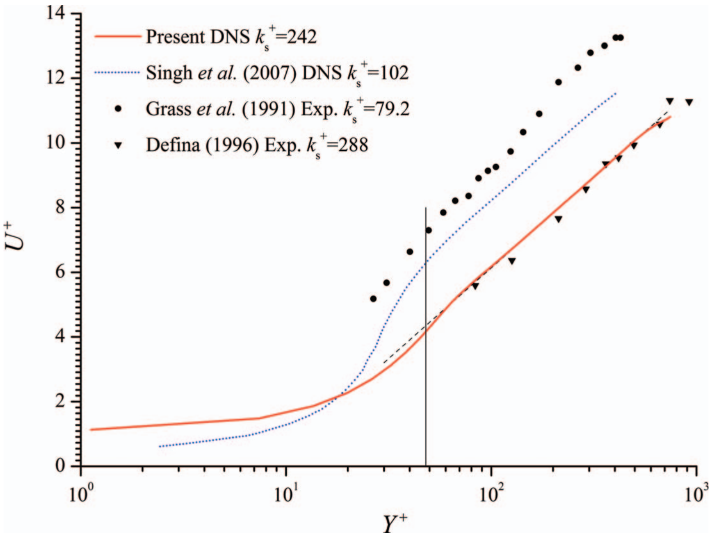

FIG. 2. Mean velocity profiles. The dashed line indicates the logarithmic law-of-the-wall with $k_s^+ = 242$ and the vertical solid line represents the highest crest of the roughness elements.

In order to compare the DNS results with those from the literature, a vertical coordinate $Y = y - y_b$ is defined. Figure 2 shows the mean stream-wise velocity profile above the effective bed location. Good agreement with the measured data of Defina[32] with roughness Reynolds number $k_s^+ = 288$ has been achieved. The deviations from the experimental data of Grass *et al.*[31] and the DNS results of Singh *et al.*[18] are obviously due to the different roughness adopted. However, these profiles collapse when they are plotted against Y/k_s, as shown in Fig. 3.

Figure 4 shows the turbulence intensities together with the experimental values from Grass[29] and Nezu[30] and the DNS results of Singh *et al.*[18] with roughness Reynolds numbers of 74.5, 100, and 102, respectively. It can be seen that the present values are lower than the experimental data of Grass[29] and Nezu,[30] but show fairly good agreement with the DNS results of Singh *et al.*[18] everywhere except near the rough-bed. The peak value of 1.84 of the stream-wise velocity fluctuation

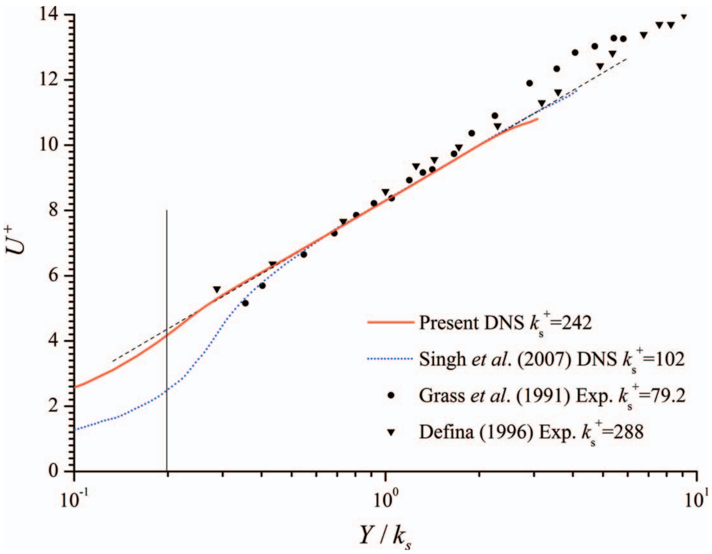

FIG. 3. Mean velocity profiles plotted against Y/k_s. The dashed line indicates the logarithmic law-of-the-wall with $k_s^+ = 242$ and the vertical solid line represents the highest crest of the roughness elements.

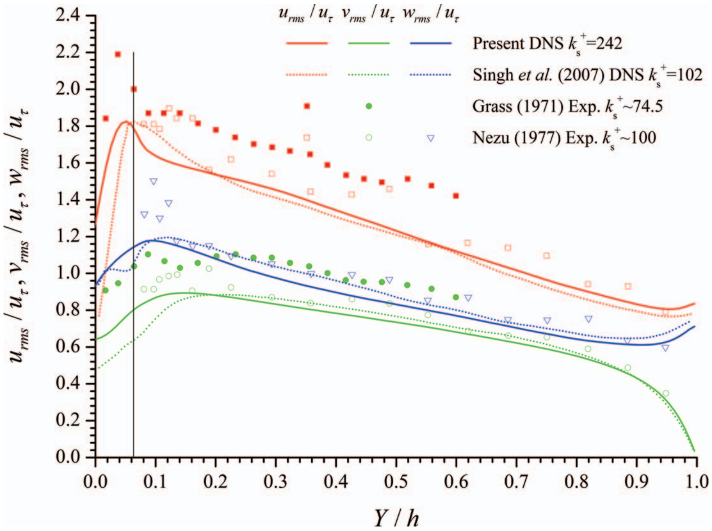

FIG. 4. Turbulence quantities. The vertical solid line represents the highest crest of the roughness elements.

u_{rms}/u_τ compares well with 1.83 obtained by Singh *et al.*[18] but both are lower than the published experimental results, e.g., $u_{rms}/u_\tau = 2.2$ in Grass,[29] and is due to the different definitions of u_τ used. In the experimental work of Grass,[29] u_τ is defined as the friction velocity on the effective bed location of a rough-bed. However, in the DNS study of Singh *et al.*[18] u_τ is calculated as $\sqrt{\tau_b/\rho_f}$, where τ_b is the shear stress estimated using a linear extrapolation of the total shear stress profile to the smooth channel bed. In this study, the definition of Singh *et al.*[18] is used for the convenience of comparison. However, if Grass's definition is used the peak values of u_{rms}/u_τ become 2.05 and 2.13, respectively, for Singh *et al.*[18] and the present simulation thus giving much closer agreement. Correspondingly, the corrected grid resolution of the present study becomes 5.4 wall units in all three directions. It should also be mentioned that these peak values are significantly lower than the values of around 2.8 for turbulent flow over smooth wall. As stated in Jiménez,[34] large roughness elements destroy the near-wall cycles of coherent flow and thus result in a reduced near-wall peak. Moreover, the random arrangement of spheres used in this study further contributes to a lower peak value due to the irregular rough-bed surface having a similar effect to large roughness elements in destroying near-wall coherent structures.

As can be seen in Fig. 4, the two DNS results agree closely with one another except near the top of the rough-bed where the peak of the stream-wise turbulence intensity in the present results shifts towards the rough-bed. The stream-wise turbulence intensity is at its maximum at a position between the effective rough-bed location and the highest crests of the spheres rather than at the top of the roughness elements in the DNS results of Singh *et al.*[18] The reason for this is most likely due to the fact that in the present study the rough-bed consists of 2-3 layers of randomly arranged spheres, rather than one layer of hexagonally arranged spheres adopted by Singh *et al.*[18]

Figure 5 shows the comparison of the Reynolds shear stress and total shear stress. The indiscernible difference between the total shear stress and the inclined straight line away from the roughness elements confirms that the turbulent flow is indeed fully developed. The peak values of the Reynolds shear stress and the total shear stress occur at $y/d = 0.322$ ($Y^+ = 70$) and $y/d = 0.303$ ($Y^+ = 51$), respectively, which are slightly higher than $y/d = 0.29$ ($Y^+ = 48$) and $y/d = 0.26$ ($Y^+ = 34$) in the study of Singh *et al.*[18]

To further verify the qualities of the above DNS results, a DNS with double grid resolution in all three directions was also carried out for turbulent flow over the fixed rough-bed only. Here, we refer to the original DNS as the 16^3 DNS and the new DNS as the 32^3 DNS due to a sphere being resolved by 16^3 and 32^3 grid points in these simulations, respectively. The grid resolutions for the 32^3 DNS was $\Delta x^+ = \Delta y^+ = \Delta z^+ = 3.125$ in wall units and Fig. 6 shows a comparison of turbulent

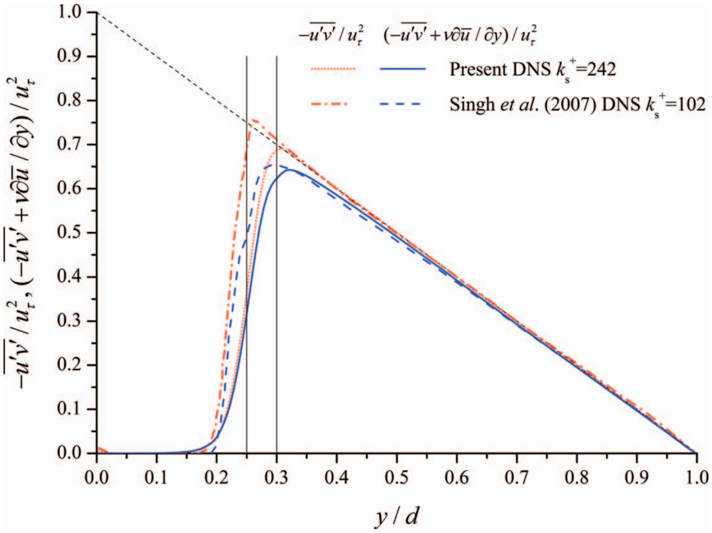

FIG. 5. Normalized Reynolds shear stress $-\overline{u'v'}/u_\tau^2$ and normalized total shear stress $(-\overline{u'v'} + \nu\partial\bar{u}/\partial y)/u_\tau^2$. The dashed inclined line represents the profile of total shear stress for fully developed smooth wall flow. Solid vertical lines denote the top of the roughness elements. The right-hand side one is for the present study and the one on the left is for the study of Singh *et al.*[18]

intensities between the 16^3 and 32^3 DNS results where it can be seen that the difference is virtually indiscernible and thus confirming that the 16^3 DNS results are grid-convergent.

C. Statistical features of the rough-bed flow with dispersed phase

Following statistically stable turbulence, the spheres were set free and their entrainment together with the surrounding flow field was recorded for a further $12T$. For the purpose of differentiating particle entrainment and particle fluctuations near balanced positions, only those spheres with a velocity greater than $0.1u_\tau$ were considered to be entrained and included in the statistical calculations. Moreover, the spheres with their center below $y/d = 0.1$ were fixed to the bottom bed. Thus, there are three kinds of spheres in the channel, i.e., the fixed spheres (below $y/d = 0.1$), the stationary

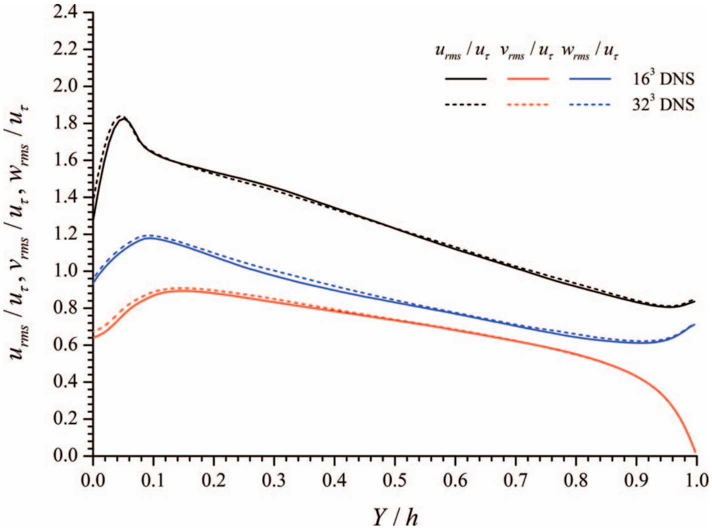

FIG. 6. Comparison of turbulence quantities between the 16^3 and 32^3 DNS results.

TABLE II. Mean flow features obtained from the DNS data for the two-phase flow.

Flow variables	Related Reynolds number
Equivalent roughness, $k_s = 0.834k$[a]	$k_s^+ = k_s u_\tau/\nu = 292$
Effective channel depth, $h = d - y_b = 2.103k$	$Re_h^+ = u_\tau h/\nu = 736$
Bulk mean velocity, $U_b = 8.259u_\tau$	$Re_b^+ = U_b h/\nu = 6079$
Mean velocity of the top surface, $U_c = 10.43u_\tau$	$Re_c^+ = U_c h/\nu = 7676$

[a] $k = 0.35d$.

(including fluctuating) spheres, and the moving spheres (both above $y/d = 0.1$). It should be noted that some spheres above $y/d = 0.1$ are always stationary due to their positions and the shielding effects of surrounding spheres while others switch between stationary and moving states. Those stationary spheres, together with the fixed spheres, form a statistically stable rough-bed.

In reality, sediment entrainment/movement only exists near the bed surface and the bed is immobile further below. The depth from the effective bed surface to the immobile bed depends upon the Shields function and other flow conditions. To mimic the immobile bed, Chan-Braun *et al.*[15] fixed the bottom layer of spheres and roughened an impermeable bed using hemi-spherical caps. For the current simulation, their approach was difficult to apply due to the random sphere arrangement and thus only the bottom layer of spheres was fixed. The side-effect of this treatment on sediment entrainment is considered to be small owing to the use of a Shields number just above the threshold and thus restricting movement to the spheres exposed to the outer flow.

To facilitate the following analysis and discussion, the following terminology is adopted: single-phase flow indicates the turbulent channel flow over the fixed rough-bed (as discussed in Sec. III B) and two-phase flow denotes the turbulent channel-flow with sediment entrainment. The fluid phase of the two-phase flow represents the flow in the whole computational domain excluding the volume occupied by spheres regardless of their state of motion while the dispersed phase of the two-phase flow is the moving spheres.

The effective bed location y_b and equivalent bed roughness k_s were again determined using the same method described in Sec. III B. However, k is uncertain in the two-phase case owing to the changing value of the highest crests of the spheres. Different values of k from zero to $0.5d$ were tried and $k = 0.35d$ was found to give the best curve-fitted results resulting in $y_b = 0.754k$ and $k_s = 0.834k$. The roughness Reynolds number for the two-phase case becomes $k_s^+ = 292$. Table II lists these values together with other mean properties computed based on the DNS data.

As can be seen in Fig. 7, a mean velocity lag between the fluid and dispersed phases is observed. This velocity lag is well documented in experiments[35–39] with different combinations of flow and particle parameters as well as the numerical simulations of Chan-Braun *et al.*[15] However, in the DNS study of Chan-Braun *et al.*,[15] the entrained particles are distributed all over the channel depth whereas in the present DNS the highest position that spheres' center can reach is about $y/d = 0.465$ partly due to the Shields function being just above the entrainment threshold. If we closely investigate the velocity profile of the dispersed phase, we can see a fluctuation in the upper part due to an insufficient sample of spheres visiting this area. Moreover, the mean particle stream-wise velocity is almost zero below $y/d = 0.2$, and thus the movement of spheres below this level are mainly fluctuations near balanced positions and verifies the rationality of fixing the bottom layer.

Figure 7 also compares the mean stream-wise velocity profiles of single-phase flow and two-phase flow cases. The modifications to the stream-wise velocity profile of fluid phase due to the presence of the dispersed phase are obvious. Above the highest crests of bed particles of the single-phase flow case, the presence of entrained particles retards the mean velocity compared with that of the single-phase flow case. Below this level, the fluid velocity is accelerated due to the moving spheres causing less momentum exchange with the fluid phase. Above $y/d = 0.465$ ($Y^+ = 201$), the momentum exchange ceases to exist and the velocity profile of fluid phase verifies the logarithmic law-of-the-wall, as shown in Fig. 8. However, a downward shift is observed comparing with the fluid velocity profile of single-phase flow.

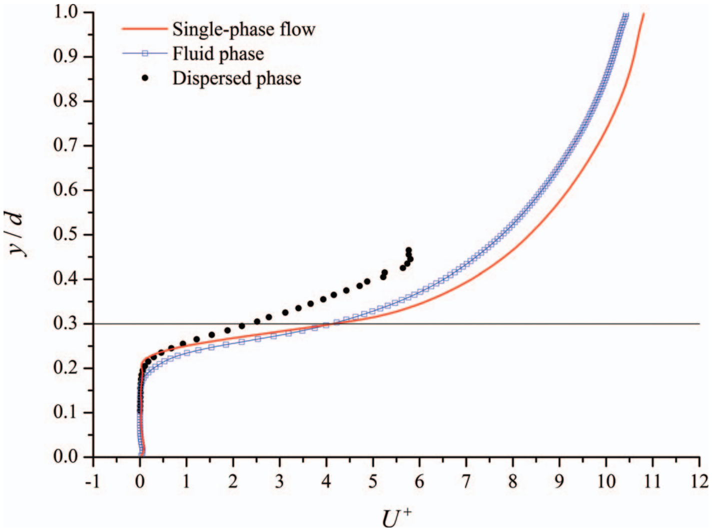

FIG. 7. Comparison of the mean stream-wise velocity profiles. The horizontal solid line denotes the top of the roughness element in the single-phase flow case with $k_s^+ = 292$.

In order to show the sediment concentration profile, the channel is divided vertically into slots of height $0.1D$. The sediment concentration C in each slot was calculated as the ratio of the volume occupied by spheres and the volume of the slot and the volume flux density q was calculated as the product of sediment concentration C and the mean stream-wise dispersed phase velocity U_p^+. Figure 9 compares the sediment concentration profile and the volume flux density with those of Durán *et al.*[40] in which the sediment transport was studied by using a discrete element method for particles coupled to a continuum Reynolds averaged description of hydrodynamics. In Fig. 9, C and q are normalized by C_s and $\sqrt{gD}$, where C_s is the static bed mean concentration. The well-documented trend that C and q decrease exponentially with height in the outer flow is clearly shown and the discrepancy between the two sets of results is due to the different values of the Shields function Θ used. In the high-Θ case of Durán *et al.*[40] Θ is approximately 1.5 times as large as the sediment entrainment threshold, which results in a larger flux density and an upward shift in its peak. The inset of

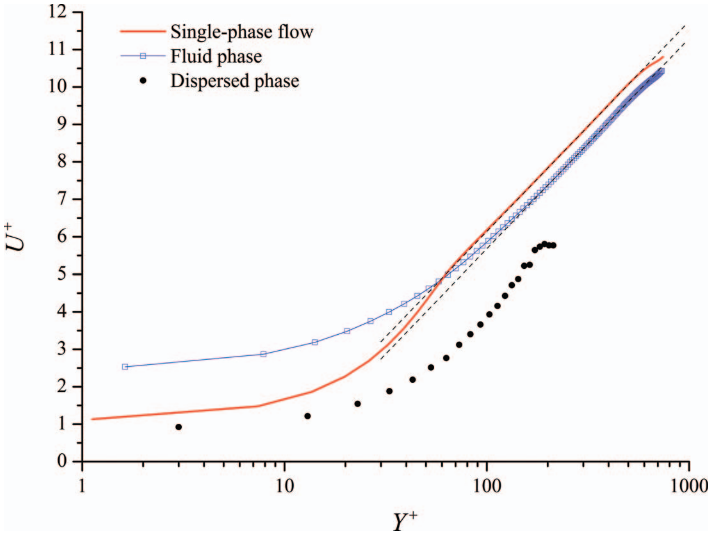

FIG. 8. Comparison of the mean stream-wise velocity profiles. The upper and lower dashed lines represent the logarithmic law-of-the-wall with $k_s^+ = 242$ and $k_s^+ = 292$, respectively.

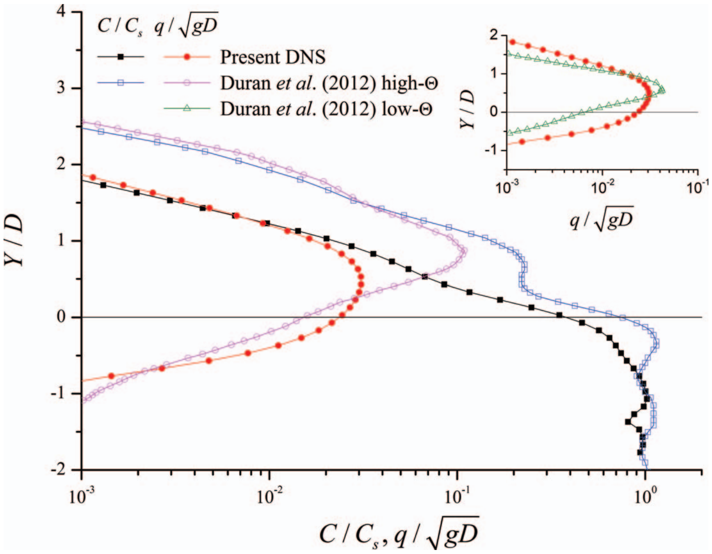

FIG. 9. Comparison of the sediment concentration and the volumetric flux density profiles with the numerical results of Durán *et al.*[40] in the dispersed phase. The horizontal solid line denotes the effective bed location.

Fig. 9 compares the authors results with those of the low-Θ case of Durán *et al.*[40] in which a Shields number just above the threshold is adopted and reasonably good agreement is observed between the two. The sediment concentration profile for this low-Θ case is not provided in Durán *et al.*[40]

The volumetric sediment flux $q_s = \int_0^d q(y)dy$ is calculated to be 0.0111 whereas if it is calculated according to $q_s = \pi D^3/(6A)\sum_p \overline{u}_p^+$, where A is the channel area and $\sum_p \overline{u}_p^+$ is the sum of mean particle velocity over all spheres, it becomes 0.0114. The non-dimensional volume flux $\phi = q_s/\sqrt{(\rho_s/\rho_f - 1)gD^3}$ is 0.0327 which agrees well with experimental data and several well-known bed-load transport equations' values, ranging from 0.01 to 0.04, at $\Theta = 0.065$ compiled by Wiberg and Smith[41] (refer to Fig. 7 of their work). It should be noted that U_p^+ indicates the mean stream-wise velocity of the dispersed phase in a horizontal slot whereas $\overline{u}_p^+$ represents the mean stream-wise velocity of an individual particle.

Figure 10 shows the turbulence quantities both for the single-phase flow and two-phase flow cases, in which the modification due to the presence of the dispersed phase is clearly seen. The near-wall peak of the stream-wise component u_{rms}/u_τ is smoothed and decreases slightly. This is in agreement with the experimental results of Kiger and Pan[37] and the numerical results of Chan-Braun *et al.*[15] The profiles of the fluctuations in the vertical and span-wise directions increase in the near-wall region although Chan-Braun *et al.*[15] found this increase to be less pronounced—possibly due to their smaller particle size. Above $y/d = 0.4$, all three turbulence fluctuations of the fluid phase overlap with those of single-phase flow. In contrast to their counterparts in the fluid phase, the velocity fluctuations of the dispersed phase in the vertical and span-wise directions are almost equal to each other in the near-wall region. In this region, the greater occurrence of collisions leads to a more isotropic distribution of sphere fluctuation energy in the vertical and span-wise directions and is in agreement with the findings of Chan-Braun *et al.*[15] However, the rough-bed may also contribute to an isotropic distribution. In the results of Chan-Braun *et al.*[15] an isotropic distribution of vertical and span-wise particle velocity fluctuations existed in a thin near-wall region ($y_d < y < y_d + D$, where y_d is their effective bed location and $D = 0.05$ is their grain-size) in which the occurrence of particle-rough bed collisions is large and the effect of the roughness elements (fixed spheres) on the particle velocity fluctuations cannot be ignored. Above this region, although the particle-particle collision likelihood is not substantially changed, particle-rough bed collisions are rare, and the span-wise fluctuation is obviously larger than the vertical one. Clearly, the weakened rough-bed effects above the region cause this phenomenon. The same trend is also demonstrated in the present results, as shown in Fig. 10. However, the isotropic region is much wider and is due to

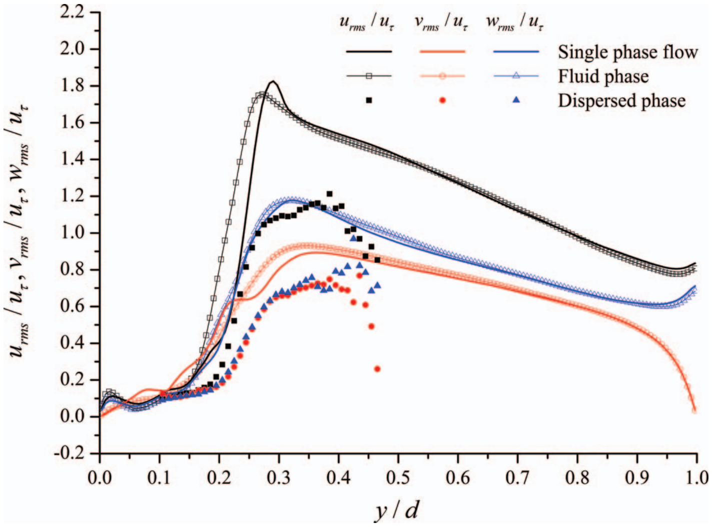

FIG. 10. Comparison of turbulence quantities between the single-phase and two-phase flow cases.

the fact that the particle Reynolds number (also the non-dimensional particle diameter) is ten times larger than that of Chan-Braun *et al.*[15]

Near the top of the dispersed phase region, the vertical velocity fluctuations of the dispersed phase plummet, but the span-wise velocity fluctuations remain high. The stream-wise velocity fluctuations decrease to the same level of the span-wise velocity fluctuations in this region although it is much larger than the span-wise and vertical fluctuations in the near-wall region. All three velocity fluctuations of the dispersed phase are consistently smaller than their fluid phase counterparts and is a result that does not agree with the findings of Chan-Braun *et al.*[15] who found that the vertical fluctuations in the dispersed phase are larger than their fluid-phase counterparts in the near-wall region. This discrepancy could be due to the lower solid-fluid density ratio, i.e., $s_s = \rho_s/\rho_f = 1.7$, and the smaller grain-size in their study—lighter and smaller particles are more easily accelerated by the surrounding flow, and are thus more turbulent.

Figure 11 compares the Reynolds shear stress and total shear stress for the single-phase and two-phase flow cases. Above $y/d = 0.4$, the difference between fluid phase data and single-phase data is indiscernible. Near the rough-bed, however, the Reynolds and total shear stresses are reduced, and the sharp transition is smoothed for the fluid phase. This is in agreement with the experimental data of Kiger and Pan[37] and the numerical results of Chan-Braun *et al.*[15]

Figure 12 shows the mean hydrodynamic forces on moving particles versus their center height. Below the effective bed location, the mean drag force F_D and mean lift force F_L are almost the same. F_D attains its peak value ($F_D/G = 0.4$, where G is the particle submerged weight) at the effective bed location and then decreases gradually. F_L has a small fluctuation at the effective bed location and reaches a plateau at about $y/d = 0.32$. The maximum of the normalized lift force is approximately $F_L/G = 0.6$ and is larger than the peak value of mean drag force. However, it should be mentioned that although F_L is smaller than G, it does not mean the instantaneous lift force on a particular particle is insufficient to lift it up. Figure 13 shows the curves of normalized standard deviations of the hydrodynamic forces and all three curves show the same trend and peak near the effective bed location although their values are different. In Fig. 14, $F_L \pm \sigma_f^L$ are plotted, where σ_f^L indicates the standard deviations of lift force. Clearly, in a relative narrow region above the effective bed location, the lift force plus its standard deviation is greater than the particle submerged weight. Above this region, although the mean lift force is higher, the lift force plus its standard deviation is smaller than a particle's submerged weight, and indicates that the direction of particle acceleration is mainly downwards.

Figure 15 shows a negatively skewed probability density function (PDF) of the fluctuating lift force f_L' for the horizontal region between $y/d = 0.25$–0.35 and the vertical line indicates the

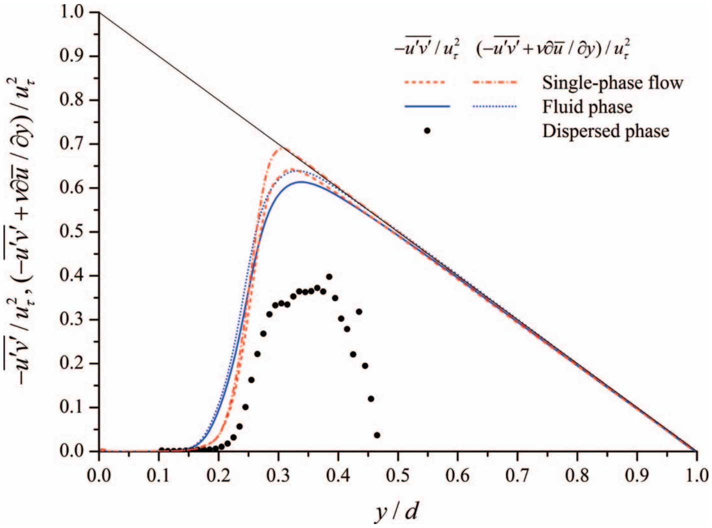

FIG. 11. Normalized Reynolds shear stress $-\overline{u'v'}/u_\tau^2$ and normalized total shear stress $(-\overline{u'v'} + \nu\partial\bar{u}/\partial y)/u_\tau^2$. The inclined solid line represents the profile of total shear stress for fully developed smooth wall flow.

submerged particle weight G. The mean lift force is $F_L = 0.373G$ and its standard deviation is $\sigma_f^L = 0.752G$. The cumulative probability of the shaded area to the right of the vertical line is 0.021 which is in good agreement with the calculated value of 0.022 (with $\Theta = 0.065$) of Wu and Chou[42] who studied the entrainment of uniformly sized particles with random grain protrusion using an entrainment probability model. This result implies that more than 2% of sediment particles will be entrained by the flow—a phenomenon classified as "small-portion sediment entrainment."

From the above, it is concluded that although the mean lift force is insufficient to lift-up the spheres in this study, the fluctuating lift force does have the necessary capability and, from a hydrodynamics point of view, this presents strong evidence of the close relationship between turbulence structures and sediment entrainment.

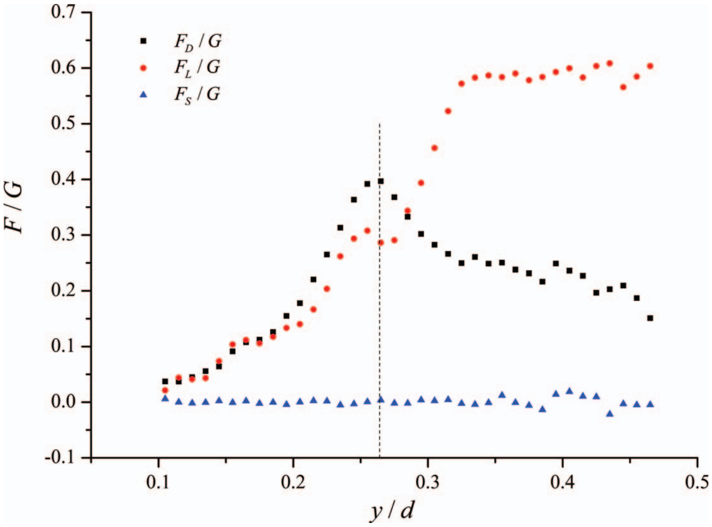

FIG. 12. Normalized mean hydrodynamic forces for the dispersed phase. The dashed vertical line indicates the effective bed location.

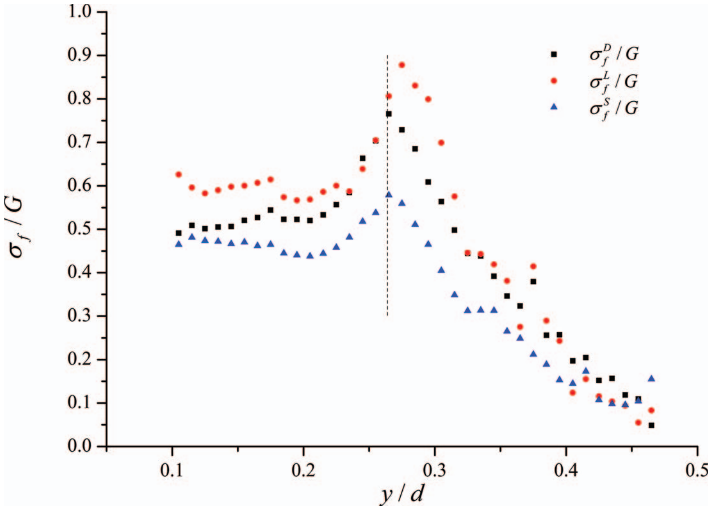

FIG. 13. Normalized standard deviations of hydrodynamic forces on the dispersed phase. Dashed vertical line indicates the effective bed location.

D. Correlation between the sediment entrainment and sweep structures

Our attention is now turned to the instantaneous behavior of the spheres and the surrounding flow field. Figure 16 shows a plan view of the arrangement of the spheres and the pressure distribution on their surfaces—red indicates high-pressure and blue the low-pressure.

Let us focus on a smaller region indicated by the box shown in Fig. 16 which contains a representative high-pressure region. In the perspective view of Fig. 17(a), the spheres are made visible by utilizing the zero contour surface of the wall distance of grid points from the sphere boundaries. The pressure distribution is then plotted on this surface. A stream-wise and a span-wise section crossing the high-pressure region, are also plotted to show the flow velocity and pressure distribution, not only over the rough-bed but also inside the sphere gaps.

Figure 17(b) shows a stream-wise plot of a typical sweep structure: $u' > 0$ and $v' < 0$ where u' and v' are the flow velocity fluctuations in the stream-wise and vertical directions, respectively. The flow dives into the sphere gaps upstream of the sphere that is about to be entrained (sphere 1).

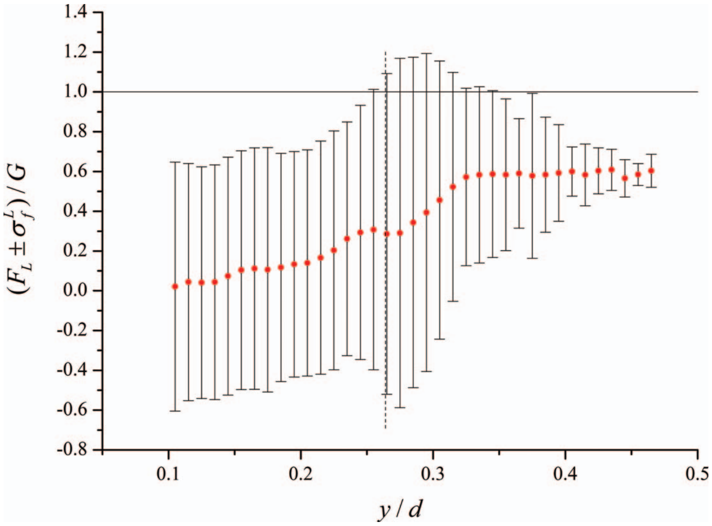

FIG. 14. Mean lift force plus/minus standard deviations for the dispersed phase. The dashed vertical line indicates the effective bed location.

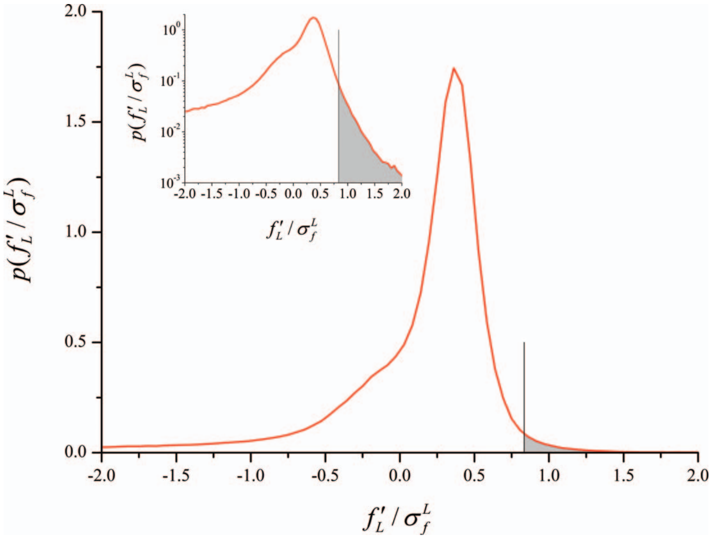

FIG. 15. The probability density function (PDF) of the fluctuating lift force f'_L for the vertical position $y/d = 0.25$–0.35. The vertical line indicates an equilibrium state where the instantaneous lift force is equal to the submerged particle weight. The shaded area is equal to the probability of sediment entrainment. The inset is a semi-logarithmic plot of the PDF.

This ready-to-move sphere is referred to as the target sphere hereafter. The high-speed flow is obstructed by the closely packed spheres which causes a relatively higher pressure under the target sphere. In some cases, the high pressure region caused by stronger sweep events can even reach the impermeable bed. Dey and Papanicolaou[43] state that the force and moments on the particles imposed by shear stresses have a negligible effect on particle dynamics in fully rough turbulent flow and that the surrounding pressure gradients determine the movement of large sediment particles. Owing to the high pressure on the windward and bottom surfaces (see Fig. 17(b)), the target sphere is lifted up and then moved downstream. This process is clearly shown by the time history of the coordinates and velocities of the target sphere in Fig. 18. In this figure, the left dashed vertical line at about $t = 0.87T$ indicates the instance in time when the target sphere is about to be entrained. There are occasions in which the target sphere moves but is not entrained because these movements are not continuous and are on a small scale, possibly from one balanced position to another one depending upon the arrangement of surrounding spheres.

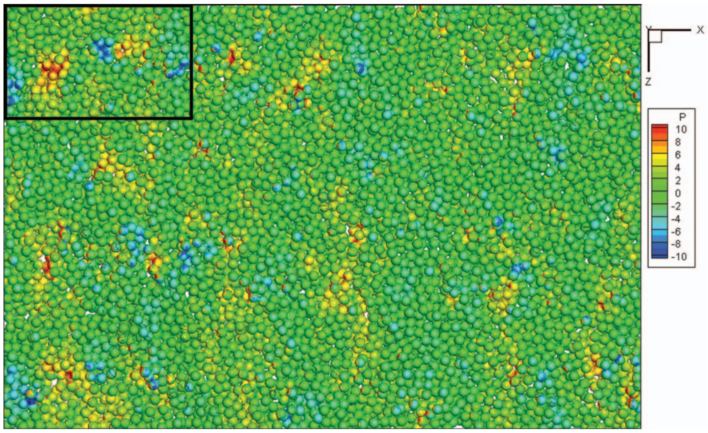

FIG. 16. A plan view of the arrangement of the spheres and their surface pressure. Red indicates high pressure and blue low pressure.

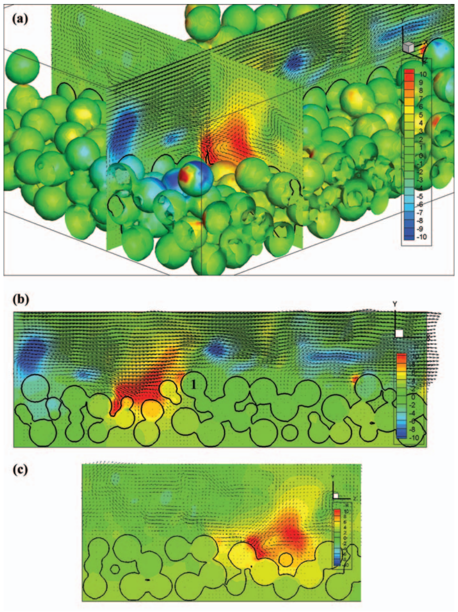

FIG. 17. A perspective view (a) of the flow fields, together with (b) $x - y$ and (c) $y - z$ section plots, at the inception of the entrainment by sweep structures of the target sphere (sphere 1). The color indicates pressure and velocity vectors are plotted every two grid points.

In order to investigate the correlation between the instantaneous fluid velocity and the spheres' movements, the time history of stream-wise and vertical velocity components of fluid flow are also shown. These were taken at a point located at $(-0.75D, 0.65D)$ relative to the center of the target sphere as Xingkui and Fontijn[44] found maximum correlation between the instantaneous flow velocity and the drag force at this position. Dwivedi *et al.*[8] also used this configuration in their entrainment experiments and found a close relationship between sweep events and particle entrainment. It can be seen from Fig. 18 that at the instance of the target sphere's entrainment, the instantaneous vertical velocity at the given point is negative while the instantaneous stream-wise velocity is relatively larger than its mean value (indicated by a dashed horizontal line), thus indicating a typical sweep event. This process was repeated a very many times in the simulation and agrees closely with the experiments of Dwivedi *et al.*[8] in which the target sphere is lifted up by a distinct sweep structure.

It is worth noting that the target sphere does not often move alone and that a cluster of spheres can be expelled off the bed in a sweep event—see Fig. 19. The span-wise scale of the entrained

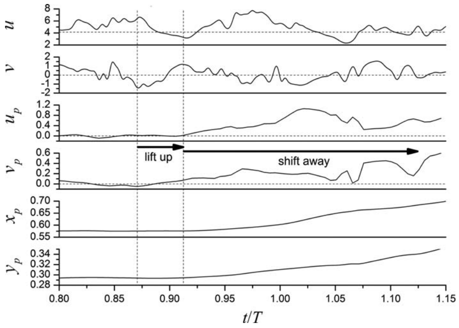

FIG. 18. Time histories of the coordinates and velocities of the target sphere and the fluid velocity at a point $(-0.75D, 0.65D)$ relative to the center of the target sphere (sphere 1). $T = d/u_\tau$ is the large-eddy turnover time, u and v are the stream-wise and vertical fluid velocity components at the given point, respectively. u_p and v_p are the stream-wise and vertical velocity components of sphere 1, respectively. x_p and y_p are the coordinates of sphere 1's center.

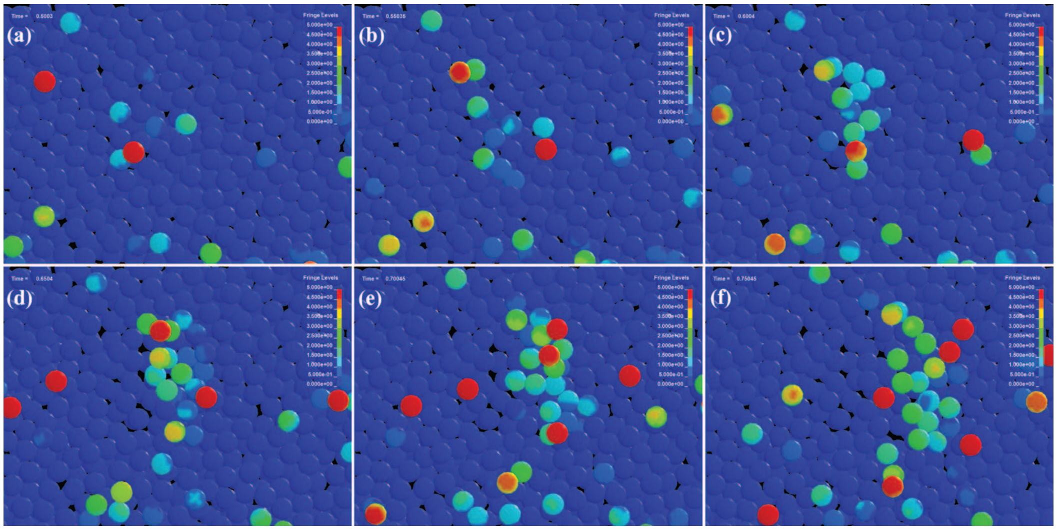

FIG. 19. (a)–(f) Sequence of sediment entrainment of a cluster of spheres. The whole time span of the sequence is $0.25T$ with a time interval of $0.05T$ between two successive sub-plots. Flow is from the left to right and the color indicates velocity magnitude of the spheres.

cluster is over 10 times larger than the spheres' diameter, i.e., about 1000 in wall units. Also, the spheres are scattered instead of aggregating along quasi-stream-wise low-velocity streaks as in the study of Niño and García,[4] Lelouvetel *et al.*,[5] and Escauriaza and Sotiropoulos.[13] The spheres just below the sweep structure are less likely to be lifted up compared to the spheres at the downstream margin of the high-pressure region possibly because the high pressure on the top of these spheres caused by the diving flow pins them to the rough-bed.

IV. CONCLUSIONS

In this paper, a numerical investigation into the correlation between turbulent coherent structures and the entrainment of individual coarse particles on the rough-bed of an open channel has been carried out using a combination of DNS, FDEM, and IBM. A simulation with a fixed rough-bed was first of all ran and mean velocity and turbulence profiles were verified against published experimental data and other available numerical results. Good agreement was achieved and once the turbulence became statistically stable, the spheres were set free and their movement and the surrounding flow fields were recorded. Various statistics of the two-phase flow were then calculated based on the DNS data. A comparison between the two-phase and the single-phase flow shows a velocity lag in the fluid phase and that there is a strong interaction between the fluid and dispersed phases near the effective bed location. The entrainment results clearly show a close relationship between continuous particle movements and sweep events. The mechanism of sediment entrainment is discussed and it was found that pressure gradients play a much more crucial role in this dynamic process than shear stresses—a conclusion that is in agreement with other studies and may be due to the large grain-size used. It was also found that particles tend to be entrained in clusters and that they are more readily entrained at the downstream margin of the high pressure region of a sweep structure.

ACKNOWLEDGMENTS

This research was supported by a Marie Curie International Incoming Fellowship within the 7th European Community Framework Programme (Grant No. PIIF-GA-2009-236457). The first author acknowledges the financial support of the Science Fund for Creative Research Groups of the National Natural Science Foundation of China (Grant No. 51021004), National Natural Science Foundation of China (Grant Nos. 50809047 and 51009105), and Natural Science Foundation of Tianjin (Grant

No. 12JCQNJC02600). We appreciate the valuable suggestions from Professor Wim Uijttewaal of TU Delft, the Netherlands and are grateful to the UKTC for HECToR computer time and facilities.

[1] R. G. Jackson, "Sedimentological and fluid-dynamic implications of the turbulent bursting phenomenon in geophysical flows," J. Fluid Mech. **77**, 531–560 (1976).

[2] B. M. Sumer and B. Oguz, "Particle motions near the bottom in turbulent flow in an open channel," J. Fluid Mech. **86**, 109–127 (1978).

[3] B. M. Sumer and R. Deigaard, "Particle motions near the bottom in turbulent flow in an open channel. Part 2," J. Fluid Mech. **109**, 311–337 (1981).

[4] Y. Niño and M. H. García, "Experiments on particle-turbulence interactions in the near-wall region of an open channel flow: Implications for sediment transport," J. Fluid Mech. **326**, 285–319 (1996).

[5] J. Lelouvetel, F. Bigillon, D. Doppler, I. Vinkovic, and J. Y. Champagne, "Experimental investigation of ejections and sweeps involved in particle suspension," Water Resour. Res. **45**, W02416, doi:10.1029/2007WR006520 (2009).

[6] B. Hofland, "Rock and roll, turbulence-induced damage to granular bed protections," Ph.D. dissertation (Delft University of Technology, 2005).

[7] S. M. Cameron, "Near boundary flow structure and particle entrainment," Ph.D. dissertation (University of Auckland, 2006).

[8] A. Dwivedi, B. Melville, and A. Y. Shamseldin, "Hydrodynamic forces generated on a spherical sediment particle during entrainment," J. Hydraul. Eng. **136**, 756–769 (2010).

[9] A. Dwivedi, B. W. Melville, A. Y. Shamseldin, and T. K. Guha, "Flow structures and hydrodynamic force during sediment entrainment," Water Resour. Res. **47**, W01509, doi:10.1029/2010WR009089 (2011).

[10] Y. S. Chang and A. Scotti, "Entrainment and suspension of sediments into a turbulent flow over ripples," J. Turbul. **4**, N19 (2003).

[11] Y. S. Chang and A. Scotti, "Turbulent convection of suspended sediments due to flow reversal," J. Geophys. Res. **111**, C07001, doi:10.1029/2005JC003240 (2006).

[12] I. Vinkovic, D. Doppler, J. Lelouvetel, and M. Buffat, "Direct numerical simulation of particle interaction with ejections in turbulent channel flows," Int. J. Multiphase Flow **37**, 187–197 (2011).

[13] C. Escauriaza and F. Sotiropoulos, "Lagrangian model of bed-load transport in turbulent junction flows," J. Fluid Mech. **666**, 36–76 (2011).

[14] C. Chan-Braun, M. García-Villalba, and M. Uhlmann, "Force and torque acting on particles in a transitionally rough open-channel flow," J. Fluid Mech. **684**, 441 (2011).

[15] C. Chan-Braun, M. García-Villalba, and M. Uhlmann, "Direct numerical simulation of sediment transport in turbulent open channel flow," *High Performance Computing in Science and Engineering '10*, edited by W. E. Nagel, D. B. Kröner, M. Resch (Springer-Verlag, Berlin Heidelberg, 2011), pp. 295–306.

[16] R. Glowinski, T. W. Pan, T. I. Hesla, and D. D. Joseph, "A distributed Lagrange multiplier/fictitious domain method for particulate flows," Int. J. Multiphase Flow **25**, 755–794 (1999).

[17] T. G. Thomas and J. J. R. Williams, "Development of a parallel code to simulate skewed flow over a bluff body," J. Wind. Eng. Ind. Aerodyn. **67–68**, 155–167 (1997).

[18] K. M. Singh, N. D. Sandham, and J. J. R. Williams, "Numerical simulation of flow over a rough bed," J. Hydraul. Eng. **133**, 386–398 (2007).

[19] J. Ma and J. J. R. Williams, "Implication of horizontal force moments for the threshold of bed entrainment in an open-channel flow," J. Hydro-Environ. Res. **3**, 2–8 (2009).

[20] C. S. Peskin, "Flow patterns around heart valves: A numerical method," J. Comput. Phys. **10**, 252–271 (1972).

[21] C. Ji, A. Munjiza, and J. J. R. Williams, "A novel iterative direct-forcing immersed boundary method and its finite volume applications," J. Comput. Phys. **231**, 1797–1821 (2011).

[22] A. Munjiza, D. R. J. Owen, and N. Bicanic, "A combined finite-discrete element method in transient dynamics of fracturing solids," Eng. Comput. **12**, 145–174 (1995).

[23] J. Xiang, A. Munjiza, J. P. Latham, and R. Guises, "On the validation of DEM and FEM/DEM models in 2d and 3d," Eng. Comput. **26**, 673–687 (2009).

[24] A. Munjiza and K. R. F. Andrews, "Penalty function method for combined finite-discrete element systems comprising large number of separate bodies," Int. J. Numer. Methods Eng. **49**, 1377–1396 (2000).

[25] A. Munjiza, *The Combined Finite-discrete Element Method* (John Wiley & Sons, Chichester, 2004).

[26] A. Munjiza, E. Knight, and E. Rougier, *Computational Mechanics of Discontinua* (Wiley, Chichester, 2011).

[27] A. M. Ardekani and R. H. Rangel, "Numerical investigation of particle-particle and particle-wall collisions in a viscous fluid," J. Fluid Mech. **596**, 437–466 (2008).

[28] J. A. Simeonov and J. Calantoni, "Modeling mechanical contact and lubrication in direct numerical simulations of colliding particles," Int. J. Multiphase Flow **46**, 38–53 (2012).

[29] A. J. Grass, "Structural features of turbulent flow over smooth and rough boundaries," J. Fluid Mech. **50**, 233–255 (1971).

[30] I. Nezu, "Turbulence structure in an open channel flow," Ph.D. dissertation (Kyoto University, 1977).

[31] A. J. Grass, R. J. Stuart, and M. Mansour-Tehrani, "Vortical structures and coherent motion in turbulent flow over smooth and rough boundaries," Philos. Trans. R. Soc. London, Ser. A **336**, 35–65 (1991).

[32] A. Defina, "Transverse spacing of low-speed streaks in a channel flow over a rough bed," *Coherent Flow Structures in Open Channels*, edited by P. J. Ashworth, S. J. Bennett, J. L. Best, S. J. McLelland (John Wiley & Sons, New York, 1996), pp. 87–99.

[33] I. Nezu and H. Nakagawa, *Turbulence in Open-Channel Flows* (Balkema, Rotterdam, The Netherlands, 1993).

[34] J. Jiménez, "Turbulent flows over rough walls," Annu. Rev. Fluid Mech. **36**, 173–196 (2004).

[35] D. Kaftori, G. Hetsroni, and S. Banerjee, "Particle behavior in the turbulent boundary layer. II. Velocity and distribution profiles," Phys. Fluids **7**, 1107–1121 (1995).

[36] A. Taniere, B. Oesterle, and J. C. Monnier, "On the behaviour of solid particles in a horizontal boundary layer with turbulence and saltation effects," Exp. Fluids **23**, 463–471 (1997).

[37] K. T. Kiger and C. Pan, "Suspension and turbulence modification effects of solid particulates on a horizontal turbulent channel flow," J. Turbul. **3**, N19 (2002).

[38] M. Righetti and G. P. Romano, "Particle-fluid interactions in a plane near-wall turbulent flow," J. Fluid Mech. **505**, 93–121 (2004).

[39] M. Muste, K. Yu, I. Fujita, and R. Ettema, "Two-phase flow insights into open-channel flows with suspended particles of different densities," Environ. Fluid Mech. **9**, 161–186 (2009).

[40] O. Durán, B. Andreotti, and P. Claudin, "Numerical simulation of turbulent sediment transport, from bed load to saltation," Phys. Fluids **24**, 103306 (2012).

[41] P. L. Wiberg and J. D. Smith, "Model for calculating bed load transport of sediment," J. Hydraul. Eng. **115**, 101–123 (1989).

[42] F. C. Wu and Y. J. Chou, "Rolling and lifting probabilities for sediment entrainment," J. Hydraul. Eng. **129**, 110–119 (2003).

[43] S. Dey and A. Papanicolaou, "Sediment threshold under stream flow: A state-of-the-art review," KSCE J. Civ. Eng. **12**, 45–60 (2008).

[44] W. Xingkui and H. L. Fontijn, "Experimental study of the hydrodynamic forces on a bed element in an open channel with a backward-facing step," J. Fluids Struct. **7**, 299–318 (1993).